Catalysis Science & Technology

ROYAL SOCIETY OF CHEMISTRY

PAPER

View Article Online
View Journal | View Issue

Cite this: *Catal. Sci. Technol.*, 2025, **15**, 5101

# Activation strategies for rice husk biochar: enhancing porosity and performance as a support for Pd catalysts in hydrogenation reactions†

Lilia Longo,[a] Davide Baldassin, *[a] Alessandro Di Michele, [b] Carla Bittencourt, [c] Federica Menegazzo [a] and Michela Signoretto [a]

Received 28th February 2025,
Accepted 4th July 2025

DOI: 10.1039/d5cy00242g

rsc.li/catalysis

Thermolytic transformation *via* pyrolysis is a sustainable approach for valorizing agricultural and organic waste, yielding biogas, bio-oil and biochar (the gas, liquid and solid fractions, respectively). Among these, biochar stands out as a promising carbon-rich material for catalytic applications due to its surface functional groups (carboxyl, hydroxyl, amino and lactone) which facilitate the anchorage of active metal phases. However, its inherently low surface area and underdeveloped porosity often limit its effectiveness as a catalyst support. To overcome this issue, this study explores the enhancement of biochar properties through activation with various agents. Biochar derived from slow pyrolysis of rice husk, an abundant agricultural waste material, was activated using both physical (steam, $CO_2$) and chemical agents (KOH, $H_3PO_4$), yielding materials denoted as ARS, ARC, ARK, and ARP, respectively. These activated biochar materials were then employed as supports for Pd nanoparticles synthesized *via* a deposition–precipitation method, and tested in benzaldehyde (BAL) hydrogenation evaluating the conversion and yield with respect to benzyl alcohol (BALOH) and toluene (TOL). The catalysts were characterized by $N_2$ physisorption, CHNS elemental analysis, PZC, SEM, TEM, XPS, Raman spectroscopy, and MP-AES to establish structure–activity relationships. Among the tested samples, Pd/ARK, with a surface area of 2635 $m^2\ g^{-1}$ and an oxygen content of 0.15%, exhibited the highest catalytic activity (TOF = 3.22 $s^{-1}$). Moreover Pd/ARK achieved a toluene yield of 77% after 1 h, highlighting its superior performance. These findings demonstrate the potential of tailored biochar activation strategies to enhance catalyst performance, offering a sustainable approach for advanced catalytic applications.

## Introduction

Unsustainable patterns of population growth, societal development, and agricultural intensification under a linear economy model are accelerating resource depletion and global waste accumulation, thereby contributing to crises such as climate change, biodiversity loss, and shortages of food, water, and energy.[1] In this context, transitioning toward a circular economy has become imperative,[2] with sustainable waste management playing a critical role in supporting this shift.[3] Every year, approximately 140 Gt of biomass is generated.[4] However, biomass also offers a valuable alternative as a feedstock for the production of value-added products such as fuels, chemicals, and polymers. Among biomass resources, rice husk (a by-product of rice processing) emerges as an abundant and promising material, as rice is a staple food for most people worldwide, with annual production reaching approximately 700 million tons.[5] Rice husk is a lignocellulosic biomass material primarily composed of cellulose (29–42 wt%), hemicellulose (14–29 wt%) and lignin (13–34 wt%).[6] In addition, it contains a significant amount of ash in the form of silica (ranging from 12% to 23.5% by weight), which has low biodegradability and can pose environmental challenges.[7]

Biomass can be converted into value-added products through several approaches, among which is pyrolysis. This process involves the thermal decomposition of the organic matter in the absence of oxygen, resulting in the formation of three main phases: bio-oil (a dark brown organic liquid primarily composed of oxygenated compounds and water),[8,9]

---

[a] *CATMAT Lab, Department of Molecular Sciences and Nanosystems, Ca' Foscari University of Venice and INSTM RUVe, Via Torino 155, 30172, Venezia Mestre, Italy*

[b] *Department of Physics and Geology, University of Perugia, Via Pascoli, 06123 Perugia, Italy*

[c] *Chimie des Interactions Plasma-Surface (ChIPS), CIRMAP, Research Institute for Materials Science and Engineering, University of Mons, 23 Place du Parc, B-7000 Mons, Belgium*

† Electronic supplementary information (ESI) available. See DOI: **https://doi.org/10.1039/d5cy00242g**

biochar (a carbonaceous solid residue[10,11]), and biogas (mainly composed of carbon dioxide, monoxide, hydrogen and short hydrocarbons).[12]

Depending on the targeted product, pyrolysis conditions can be modulated. Fast pyrolysis, which involves heating rates exceeding 200 °C min$^{-1}$ and a residence time of a few seconds, favours bio-oil production,[6,13] while slow pyrolysis yields a higher percentage of biochar.[14,15]

Biochar is a solid material with a high carbon content. Depending on the feedstock, pyrolysis conditions, and subsequent treatments, this material can exhibit distinct characteristics, including a functionalized surface with heteroatoms, specific textural properties and high surface area. These features make biochar a versatile material suitable for various applications such as soil amendment,[14,16] adsorbents for contaminant reduction in soil and water,[17] gas adsorbents,[18] in supercapacitors,[19] and in catalysis.[20]

Biochar can be used as a catalyst in its raw form[21] or as a support for dispersing the metal active phase,[22] thereby enhancing metal, anchoring, dispersion and overall catalytic activity.[23]

High surface area is one of the most important characteristics for catalytic supports, as it provides great phase dispersion, increasing the availability of the active sites.[24]

The biochar surface area can be increased by appropriate activation steps, which involved the partial oxidation of the carbon structure, increasing the porosity of the material.[25]

There are several methods to enhance the physicochemical properties of biochar, broadly categorized into physical activation and chemical activation. Physical activation typically involves the use of gaseous oxidizing agents such as steam or $CO_2$.[26] The activation process with the two gases is slightly different; however, it works on the same principle of oxidizing the carbon structure, releasing gaseous products like CO and $CO_2$, and generating new porosity, thus enhancing the surface area.[27]

Activation with steam serves two primary functions: facilitating devolatilization and the formation of crystalline carbon, as well as removing trapped by-products of incomplete combustion from pyrolysis,[28] and reacting with the carbon skeleton leading to the development of new pores. This process significantly increases the surface area of biochar. Activation with $CO_2$, on the other hand, promotes pore formation and enhances the microporous structure, thereby improving gas adsorption properties.[29] The main reactions occurring between steam and the carbon matrix are reported in eqn (1) and (2):[30]

$$C + H_2O \leftrightarrows CO + H_2 \tag{1}$$

$$C + 2H_2O \leftrightarrows CO_2 + 2H_2 \tag{2}$$

Meanwhile for carbon dioxide, the main reaction is the Boudouard equilibrium, reported in eqn (3):[31]

$$C + CO_2 \leftrightarrows 2CO \tag{3}$$

On the other hand, chemical activation involves the impregnation of acids or bases like $H_3PO_4$, $ZnCl_2$, KOH, NaOH, *etc.* that interact with the carbon at high temperatures to modify its structure, increasing the surface area, altering the chemical composition, and introducing functional groups. Acid treatments can reduce ash content, introduce functional groups onto the biochar surface, and, depending on the type and concentration of the acid used, influence surface area.[32] Alkaline treatments aim to increase surface area and introduce oxygen-containing functional groups.[33] The reactions occurring between the carbon and the base are quite complex and they involve the formation of the oxide and carbonate and the reduction by the carbon to the metallic form. When KOH is used as an activating agent, the reaction mechanism occurring is summarized in eqn (4)–(7).[31]

$$6KOH + 2C \rightarrow 2K + 3H_2 + 2K_2CO_3 \tag{4}$$

$$K_2CO_3 \rightarrow K_2O + CO_2 \tag{5}$$

$$K_2CO_3 + 2C \rightarrow 2K\ (\text{or}\ K_2O) + 3CO \tag{6}$$

$$K_2O + C \rightarrow 2K + CO \tag{7}$$

This permits the etching in the carbon matrix, developing a deep network of pores. Also, the alkaline treatment is an effective desilication treatment,[34] thus resulting interestingly in the treatment of rice husk biochar, due to the high silica content of this biomass. Indeed, silica could be the cause of pore clogging, so the desilication could lead to pore opening.[35] Additionally, the silica extracted during activation can be utilized to produce silica-based materials, offering a more sustainable alternative to other silica sources.[36,37]

Acid activation is equally complex, though it follows a different mechanism. When phosphoric acid is used, it catalyses bond cleavage and crosslinking reactions, while the formation of phosphate radicals can lead to esterification reactions on the biochar surface.[38] Additionally, excess unreacted $H_3PO_4$ undergoes dehydration to $P_4O_{10}$, which is a highly oxidizing agent and in the temperature range of 400–700 °C reacts with carbon to form $CO_2$, widening and creating new pores, as reported in eqn (8).[39]

$$P_4O_{10} + 2C \rightarrow P_4O_6 + 2CO_2 \tag{8}$$

At higher temperatures, above 700 °C, $PH_3$ is formed, and CO and $CO_2$ are still released by the oxidation of carbon and decomposition of surface functionalities, as reported in eqn (9).

$$P_4O_{10}\ \text{or}\ P_4O_6 + CHx \rightarrow PH_3 + CO_2\ \text{or}\ CO \tag{9}$$

Furthermore, phosphorus-containing functional groups are formed on the carbon surface during activation, imparting acidic properties to the carbon[40] and increasing the hydrophilicity. Enhanced hydrophilicity can improve the interaction between the catalyst and hydrophilic molecules. However, the extent of acidity depends on the activation temperature. Higher temperatures result in reduced acidity, due to decomposition of surface functionalities. For instance, biochar activated with sulphuric acid at low temperatures (typically 80–180 °C) is used in transesterification reactions.[41] Therefore, it is essential to carefully tune the activation conditions when acids are used as activating agents, depending on the intended application of the catalysts, whether the goal is to modify the textural properties or to induce a specific chemical change on the surface.

Locally sourced biochar, when appropriately activated, can become a more sustainable alternative to conventional carbon-based catalysts.[42,43] In this work, physical and chemical activation was investigated to produce activated carbon derived from rice husk, to be employed as a support for Pd/C catalysts, which are industrially relevant catalysts for hydrogenation reactions, commonly used in the chemical and pharmaceutical industries.[44,45] One significant industrial application is their use in the purification of crude terephthalic acid (CTA), a key step in the production of polyethylene terephthalate (PET).[46] They are also effective hydrogenation catalysts for biomass-derived raw materials, such as furfural[47] or vegetable oils for the production of biodiesel.[48]

In this study, the hydrogenation of benzaldehyde was employed as a model reaction to assess the catalytic performance of various Pd/C catalysts prepared using four different activation methods: steam, $CO_2$, KOH and $H_3PO_4$.[49,50] Benzaldehyde hydrogenation is an industrially significant transformation, leading to the production of benzyl alcohol, a key intermediate in the synthesis of fragrances, preservatives, and pharmaceuticals.[51] Furthermore, the hydrogenolysis of benzyl alcohol to toluene is particularly relevant in the context of hydro-upgrading of bio-derived compounds,[52] such as aldehydes present in bio-oil, towards the production of fuel-range hydrocarbons.[53–55]

## Experimental section

### Support preparation

Rice husk (R) was supplied by Riseria delle Abbadesse, Grumolo delle Abbadesse, Vicenza, Italy. The pyrolysis was conducted in a laboratory-scale prototype plant (Carbolite custom model EVT 12/450B) as explained in previous work.[56] Briefly, 30 g of biomass was placed in a quartz tubular oven, and the pyrolysis was conducted with a heating ramp of 10 °C $min^{-1}$ till 700 °C and the temperature was held for 30 minutes under a nitrogen atmosphere (gas flow of 100 mL $min^{-1}$). After cooling, the produced rice husk biochar (BR) was collected and subsequently activated with different agents in a horizontal oven using a tubular quartz reactor similarly to the pyrolysis step.

When physical activation was performed, the char was placed in the horizontal oven and treated with a flow of 100 mL $min^{-1}$ of 1:1 $H_2O:N_2$ or pure $CO_2$ with a total flow of 100 mL $min^{-1}$ with a temperature ramp of 10 °C $min^{-1}$ until 850 °C and the temperature was kept for 90 minutes. After 90 minutes, the gases were switched to pure $N_2$ (100 mL $min^{-1}$) until the system cooled. The obtained activated char samples were labelled ARS and ARC, respectively.

When chemical activation was performed, the char was previously impregnated with the activation agent. Specifically, for KOH activation, 5 g of biochar was added to a 6 M solution of KOH (Sigma Aldrich, 85%) with a biochar:KOH mass ratio of 1:4 and stirred at room temperature for 30 minutes. The solution was dried first by heating at 80 °C to a sludge and then at 110 °C overnight. The impregnated char was placed in a tubular oven and subjected to heating under a $N_2$ flow of 100 mL $min^{-1}$ with a heating ramp of 10 °C $min^{-1}$, up to 850 °C for 90 minutes, obtaining the activated char ARK.

For $H_3PO_4$ impregnation, 5 g of biochar was added to 150 mL of a 0.7 M $H_3PO_4$ solution (prepared from 85% phosphoric acid, Sigma Aldrich), with a biochar:$H_3PO_4$ mass ratio of 1:2. The mixture was stirred at room temperature for 30 minutes, and then dried first by heating at 80 °C, evaporating the liquid until obtaining a sludge, and then at 110 °C overnight. The impregnated char was then heated to 500 °C under a flow of $N_2$ (100 mL $min^{-1}$) with a heating ramp of 10 °C $min^{-1}$ for 90 minutes. This procedure was based on a previous screening, which showed that higher activation temperatures led to excessive burn-off and a very low carbon yield. This was also validated by literature findings,[57] confirming that harsher conditions negatively affect the biochar yield and cause the collapse of the porous structure.[58,59] The obtained activated char was labelled ARP.

The different activation conditions are shown in Table 1.

After activation, the biochar samples were subjected to acidic washing with a 1 M HCl (prepared from 37% hydrochloric acid, Sigma Aldrich) solution (mass-to-volume ratio of 1 g:20 mL), to remove the alkali metals from the carbonaceous structure. The suspension was left for 60 minutes under ultrasonication. The biochar samples were then washed with distilled water until no chlorides were found ($AgNO_3$ test).

### Catalyst preparation and reaction test

The activated biochar samples were ground to a fraction of 63–40 μm and used as supports for the preparation of Pd/C catalysts by a deposition–precipitation method of $H_2PdCl_4$ (nominal Pd content of 0.75 wt%) (Janssen, 59% Pd) in $H_2O$, as explained in previous work.[56] Reduction was performed with the addition of sodium formate (Sigma Aldrich, 99%). The catalysts were then filtered and rinsed with distilled water until disappearance of chlorides by the $AgNO_3$ test and dried in an oven at 110 °C for 18 hours.

Table 1 Summary of physical and chemical activation conditions applied to rice husk biochar. All activation procedures were performed for 90 minutes

| Sample | Activation agent | Pretreatment | Flow | Activation temperature |
|---|---|---|---|---|
| ARS | Steam | — | 1:1 $H_2O:N_2$ total 100 mL min$^{-1}$ | 850 °C |
| ARC | $CO_2$ | — | $CO_2$ 100 mL min$^{-1}$ | 850 °C |
| ARK | KOH | Impregnation with 6 M KOH for 30 minutes, drying. | $N_2$ 100 mL min$^{-1}$ | 850 °C |
| ARP | $H_3PO_4$ | Impregnation with 7 M $H_3PO_4$ for 30 minutes, drying | $N_2$ 100 mL min$^{-1}$ | 500 °C |

The hydrogenation of benzaldehyde was carried out in a semi-batch reactor consisting of a three-necked round-bottom flask equipped with an external jacket connected to a Haake DC 30 thermostat for temperature control. The reactor was fitted with a hydrogen bubbler to flow gas into the solution at atmospheric pressure ($H_2$ flow: 10 mL min$^{-1}$), a condenser, and an overhead stirrer (Eurostar IKA) set to 1500 rpm to ensure efficient mixing.

In a typical catalytic test, 200 mg of catalyst was suspended in 20 mL of ethanol (>99.9% J.T. Baker) and pre-reduced *in situ* at 80 °C under a hydrogen flow (10 mL min$^{-1}$) for 60 minutes. After this activation step, the temperature was decreased to 25 °C before introducing 1 mL of benzaldehyde (>99% Sigma-Aldrich) along with an internal standard (*n*-octane, >99% Fluka).

The reaction progress was monitored by sampling the reaction mixture every 10 minutes and analysing it using an Agilent 8860 gas chromatograph equipped with a HP-5 capillary column ($L$ = 30 m, $Ø$ = 0.32 mm, film thickness = 0.25 μm) and a FID. The product identification was confirmed *via* GC/MS (EI, 70 eV) with a HP5-MS column.

The benzaldehyde conversion, product selectivity and turn-over frequency (TOF) were calculated according to the following equations:

$$\text{Conversion} = \frac{n_{\text{reacted benzaldehyde}}}{n_{\text{initial benzaldehyde}}} \times 100\% \tag{10}$$

$$\text{Selectivity} = \frac{n_{\text{product}}}{n_{\text{reacted benzaldehyde}}} \times 100\% \tag{11}$$

$$\text{TO F} = \frac{n_{\text{BAL}} + n_{\text{TOL}}}{n_{\text{Pd}} \times D \times t} \tag{12}$$

where $t$ = 10 minutes and $D$ is the palladium dispersion calculated *via* TEM using the following equation:[60]

$$D = \frac{6 \times A}{\rho \times \sigma \times L \times d_{\text{avg}}} \tag{13}$$

where $A$ = atomic mass (106.42 g mol$^{-1}$), $\rho$ = density (12.02 × 10$^6$ g m$^{-3}$), $\sigma$ = average surface area occupied by one Pd atom (0.79 × 10$^{-19}$ m$^2$) and $L$ = Avogadro's constant.

The relative error for repeated reactivity tests was less than 5%.

## Support and catalyst characterization

The CHNS elemental analysis was conducted on an Elementar UNICUBE organic elemental analyser. The total ash content was determined through total combustion following the ASTM method D2866-11,[61] while the oxygen content was determined by the difference expressed in eqn (14):

$$\%[\text{O}] = 100 - \%[\text{C}] - \%[\text{H}] - \%[\text{N}] - \%[\text{S}] - \%[\text{ashes}] \tag{14}$$

FT-IR measurements were conducted on a Perkin Elmer Spectrum One in a wave number range of 450–4000 cm$^{-1}$ with a resolution of 1 cm$^{-1}$ to study the main functional groups of the biochar before and after the different activation methods. X-ray photoelectron spectroscopy (XPS) analyses were conducted utilizing a PHI Genesis instrument manufactured by Physical Electronics (Chanhassen, MN, USA), which was outfitted with a monochromatic aluminium Kα X-ray source. The specimens were affixed to copper conductive tape that is compatible with ultra-high vacuum (UHV) conditions to facilitate charge compensation. To moderate charge accumulation during the analytical process, a dual charge neutralization technique was employed. The binding energy scale was calibrated using the C 1s peak, which was established at 284.6 eV.

Nitrogen physisorption measurements were performed on an Anton Paar Autosorb iQ to evaluate the surface area and porosity of the biochar at −196 °C after a degassing treatment at 200 °C for 6 hours.

The morphology of the carbon materials prior to and after activation was studied *via* scanning electron microscopy on an FE-SEM LEO 1525 ZEISS (Jena, DE). The acceleration potential voltage was maintained at 15 keV and measurements were carried out using an AsB detector (angle selective backscattered detector) and an In-lens detector. Elemental composition and chemical mapping were determined using a Bruker Quantax EDX. Transmission electron microscopy was used to evaluate the average particle size and distribution *via* a Thermo-Fisher Scientific TALOS F200X G2 microscope, using a magnification of 190k×. The point of zero charge (PZC) was evaluated through a pH drift method. 30 g of sample was put in 10 mL of a range of solutions of pH from 2 to 12 and the mixtures were shaken for 48 h, and then the initial pH was plotted against the final pH.[62] The actual content of palladium on the final catalyst was determined *via* microwave plasma atomic emission spectroscopy (MP-AES) using an Agilent 4210 spectrometer after acid digestion of the samples in *aqua regia* for 5 h under reflux.

Temperature-programmed desorption ($NH_3$-TPD) analyses of the samples were carried out using lab-made equipment to study the acidity of the catalysts. First, 100 mg of the catalyst was charged in a quartz reactor, reduced in 5% $H_2$/Ar

**Table 2** Elemental composition and mass ratio of elements of the non-activated and activated biochar samples from CHNS elemental analysis

| Sample | C [%] | H [%] | N [%] | S [%] | O [%] | Ash [%] | H/C ratio | O/C ratio | N/C ratio |
|---|---|---|---|---|---|---|---|---|---|
| R | 38.1 | 5.1 | 0.5 | 0.7 | 55.6 | 18.1 | 0.13 | 1.46 | 0.013 |
| BR | 50.9 | 1.3 | 0.5 | 0.3 | 2.5 | 44.5 | 0.025 | 0.05 | 0.001 |
| ARS | 48.1 | 0.6 | 0.4 | 0.3 | 3.2 | 47.4 | 0.013 | 0.07 | 0.007 |
| ARC | 47.1 | 0.8 | 0.4 | 0.1 | 3.3 | 48.3 | 0.019 | 0.07 | 0.009 |
| ARK | 91.3 | 0.1 | 0.3 | 0.3 | 0.3 | 8.0 | 0.001 | 0.002 | 0.003 |
| ARP | 33.6 | 1.3 | 0.3 | 0.1 | 2.9 | 61.8 | 0.039 | 0.09 | 0.009 |

**Table 3** Surface area and pore volume of the non-activated and activated biochar samples

| Sample | $S_{\text{Langmuir}}$ (m$^2$ g$^{-1}$) | $S_{\text{micro}}$ (m$^2$ g$^{-1}$) | $V_{\text{pores}}$ (m$^3$ g$^{-1}$) |
|---|---|---|---|
| BR | 228 | 178 | 0.08 |
| ARS | 423 | 376 | 0.18 |
| ARC | 367 | 222 | 0.11 |
| ARK | 2635 | 1337 | 0.53 |
| ARP | 112 | 64 | 0.12 |

at 80 °C and degassed in He with a flow rate of 40 mL min$^{-1}$ at 100 °C for 90 min. The catalyst was then cooled down to 25 °C prior to adsorption of ammonia. Then, the adsorption of 5% $NH_3$/He with a flow rate of 40 mL min$^{-1}$ at 25 °C for 30 min was performed. The physisorbed ammonia was removed from the catalyst surface by passing He (40 mL min$^{-1}$) at 25 °C for 10 min. The desorption profiles of $NH_3$-TPD were recorded using a thermal conductivity detector (Gow-Mac TCD) from 25 to 600 °C at a heating rate of 10 °C min$^{-1}$ under a flow of He (40 mL min$^{-1}$).

## Results and discussion

### Characterization of the supports

As evidenced by the elemental analysis reported in Table 2, the activation methods used on biochar significantly influenced its structure and chemical composition. The elemental analysis of rice husk (R) confirms its high ash content (18.1%), predominantly composed of silica,[63] which is further increased after carbonization (44.5% in BR), as the inorganic content is retained in the solid fraction of pyrolysis. The carbonization process also led to an increase of the carbon content (from 38.1% in R to 50.9% in BR), and a notable decrease of the oxygen content (from 55.6% to 2.5%), confirming the decomposition of the organic macrostructure, such as lignin, cellulose and hemicellulose, rich in oxygen, to a more ordered carbonaceous structure. Compared to BR, the different activation agents led to variations in elemental composition. The C burn-off in ARS and ARC was modest, leading to 48.1 and 47.1 C%, with slightly increased O%, with respect to BR. Chemical activation exerted a more substantial effect on the carbon matrix. Activation with KOH reduced the silica content to 8.0%, and the carbon content in ARK exceeded 90%. In fact, desilication with a strong base is a method commonly employed for producing carbon with controlled porosity using narrow-pore sized silicas as templating agents.[64] On the other hand, activation with phosphoric acid results in higher burn-off, leading to 33.6% C, but it did not affect the silica, as the ash content remained high (61.8%), indicating that silica is more resistant to the acid even at high temperatures.[65]

The hydrogen-to-carbon atomic ratio (H/C ratio) is a valuable parameter for understanding the structure and bonding characteristics of char. A low H/C ratio indicates a high aromatic content, whereas a higher ratio reflects the presence of more aliphatic carbon.[66] A decrease in the H/C ratio is observed after all the activation treatments, except for ARP, with a more marked effect on ARK, suggesting a more aromatic structure.[67]

ARP exhibited a higher hydrogen content and a lower carbon content, leading to an exceptionally high H/C ratio. This may be attributed to the lower activation temperature, which helps retain hydrogen-containing functional groups

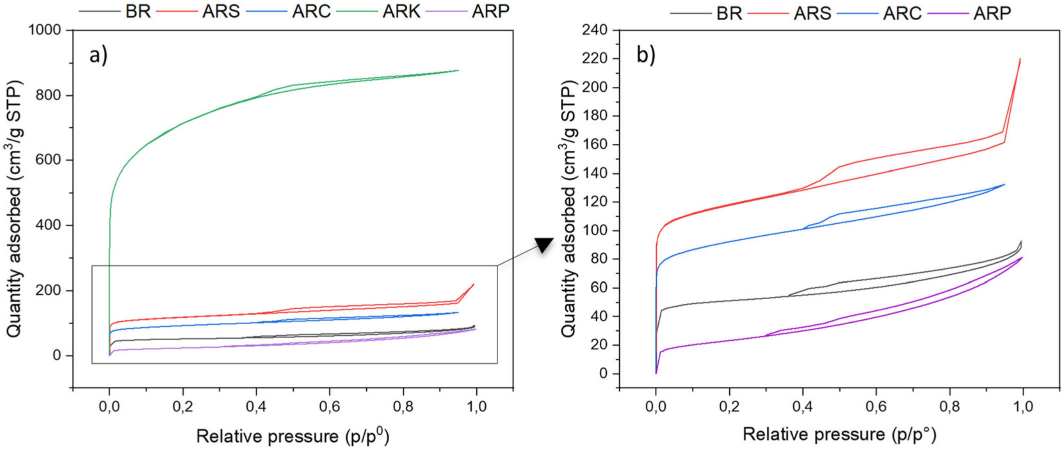

**Fig. 1** $N_2$ adsorption–desorption isotherms of the non-activated and activated biochar samples. a) All samples. b) Magnification between 0 and 240 cm$^3$ g$^{-1}$.

and aliphatic C–H bonds,[68] as well as the introduction of acid functionalities through acid activation.[69]

The sulphur content across all samples is low, particularly for ARC and ARP, which is advantageous for catalytic applications. The low sulphur content makes these materials suitable as supports for palladium nanoparticles since sulphur can poison such catalysts through surface Pd–S interactions.[70]

Nitrogen physisorption analysis was performed to evaluate and compare the surface area and pore size distribution of the biochar samples before and after activation, two critical parameters for catalytic supports.[71] The results, presented in Table 3, and the isotherms in Fig. 1, indicate that the different activation treatments had a significant impact on the surface area of the activated biochar samples. Prior to activation, BR exhibited a combination of type 1 and 4 isotherms, characteristic of materials containing both micro- and mesopores, with a surface area of 228 $m^2\ g^{-1}$. This differs from other non-lignocellulosic biomass materials such as algae, sewage sludge, and animal-derived by-products, which typically require an initial activation process to develop a porous structure.[31,56] In particular, the decomposition of cellulose and lignin leads to the formation of channels and pores, a process that in this case is further enhanced by the presence of silica.[72]

Among the activated char samples, ARK demonstrated the highest surface area (2635 $m^2\ g^{-1}$), significantly surpassing the other activated char samples. However, ARS and ARC also showed enhanced textural properties, with

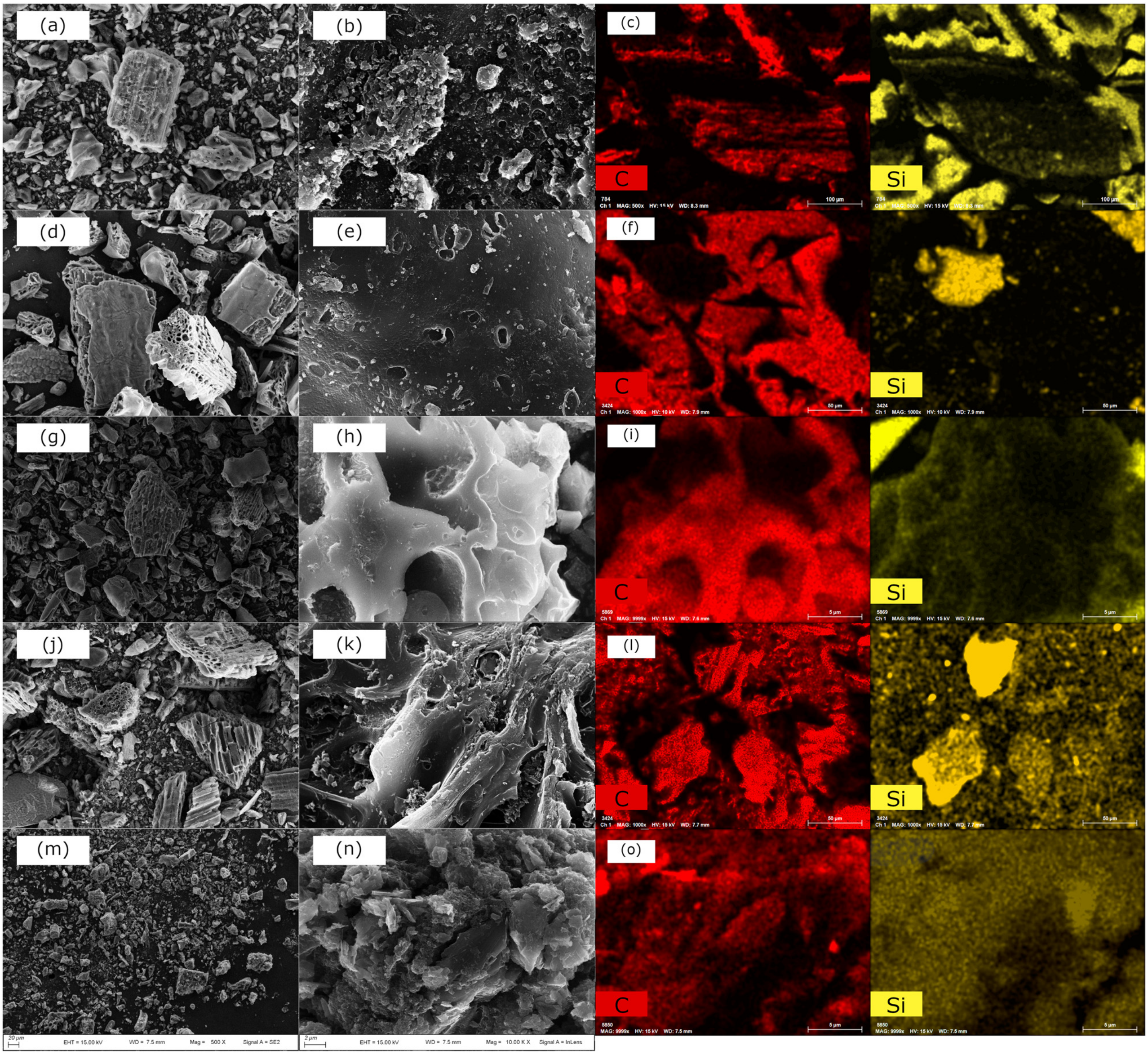

**Fig. 2** SEM images and EDX mapping (C in red, Si in yellow) of BR (a–c), ARS (d–f), ARC (g–i), ARK (j–l), and ARP (m–o) at 500 and 10k× magnification.

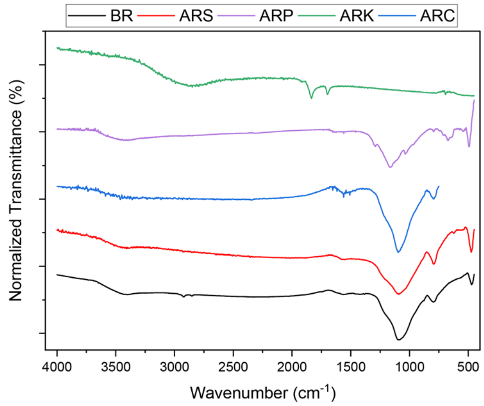

**Fig. 3** FT-IR spectra of non-activated and activated biochar samples.

values of 423 and 367 $m^2\ g^{-1}$, respectively. These values suggest that physical activation resulted in activated biochar with textural properties comparable to the pristine biochar, retaining the mixed type 1 and 4 isotherms typical of micro- and mesoporous materials.

In contrast to other activating agents, treatment with phosphoric acid led to a decrease in surface area, with ARP exhibiting a value of only 112 $m^2\ g^{-1}$. This reduction is unfavourable for the intended application, as a higher surface area and porosity could facilitate the dispersion of the active metal phase.[73] A lower carbon content in ARP registered by CHNS analysis could confirm that the sample underwent aggressive oxidation, ultimately causing structural collapse of some of the microporous region. This interpretation is supported by the reduced nitrogen adsorption at low relative pressures, in the isotherm profile.

The literature reports variable outcomes for acid activation. For instance, Cao *et al.*[32] used $H_3PO_4$ to activate pine sawdust biomass, and observed an increase of surface area at activation temperatures of 400–600 °C. Similar trends were reported by Chu and coworkers.[59] However, Iriarte-Velasco *et al.* found that $H_3PO_4$ activation of biochar derived from pork bones was less effective, emphasizing the importance of the acid-to-biochar ratio to avoid pore structure collapse.[114] Additionally, Panwar and Pawar reported that acid-modified biochar often exhibits lower surface areas compared to other activation agents, possibly because of pore structure collapse, while also showing significantly higher oxygen content,[25] consistent with our findings. Similarly, Hazmi *et al.*[74] observed a decrease in surface area when treating rambutan seed biochar with $H_2SO_4$ at 180 °C. Vaughn *et al.* reported comparable reductions in surface area, following acid treatment.[75]

Taken together, these studies highlight that the outcome of acid activation is strongly dependent on several variables, including the type of biomass, biochar characteristics, reactant ratio, and activation conditions. Even when employing relatively low temperatures, as in our case, acid treatment may not yield an increase in surface area and may instead compromise the structural integrity of the material.

SEM images, reported in Fig. 2, show that the biochar structure is preserved among the different samples, although the activated ones present a corrugated structure with increased defects, suggesting erosion from the oxidizing activation agents. All the samples exhibit a fragmented and heterogeneous structure, consistent with previous studies.[76] Notably, the activated samples feature more hollow structures with abundant channels compared to the bare biochar.[77]

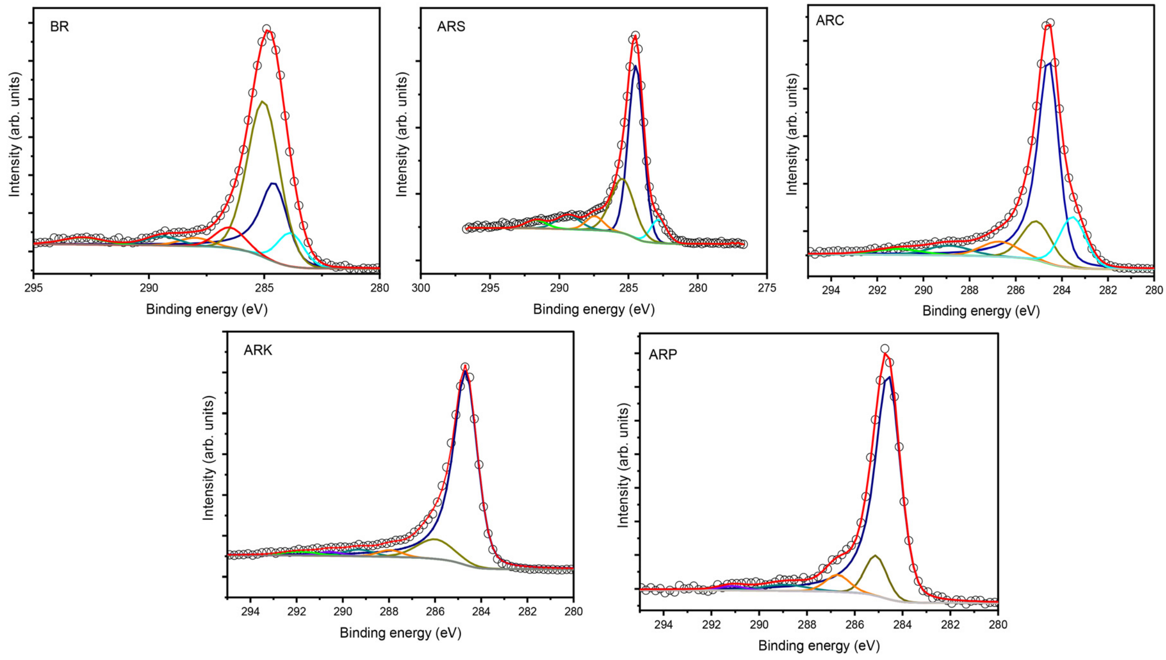

**Fig. 4** XPS spectra of non-activated and activated biochar samples.

Images at a magnification of 10.00k× indicated that ARK (Fig. 2k) displayed a more corrugated structure, with enhanced defects, while ARS and ARC (Fig. 2e and h) retained the structure of the starting biochar (Fig. 2b). ARP (Fig. 2n) instead exhibited a morphology more like silica than carbon, as confirmed by EDX analyses (Fig. 2o), which revealed a homogeneous distribution of silica throughout the sample. This suggested that the acid activation had the most significant impact on the char structure, leading to its collapse, and despite the lower activation temperature, the resulting char consisted of highly fractured small chunks.

Besides ARP, C and Si mapping highlighted the influence of the activation process on elemental distribution across all samples. In biochar samples subjected to physical activation, carbon and silica were distinctively distributed, indicating a heterogeneous material composed of alternating layers of these elements, consistent with the mapping results of non-activated biochar. In contrast, ARK showed an almost complete disappearance of silica aligning with previous characterization.

The activation process significantly influenced also the surface functionalities and composition of the biochar samples, as evidenced by FTIR and XPS, reported in Fig. 3 and 4 and Tables 4 and 7.

FT-IR analysis revealed that all the biochar samples, except ARK, exhibit characteristic silica-related peaks, including a prominent Si–O–Si stretching vibration[78] at 1090 $cm^{-1}$, along with Si–O bending and Si–O rocking vibrations at around 800 $cm^{-1}$ and 450 $cm^{-1}$, respectively.[79] The diminished intensity of these peaks in ARK suggests a significant reduction in residual ash content, further confirming the effectiveness of KOH activation as a desilication process.

This observation is supported by XPS (Table 4), which indicates that the ARK surface has the highest carbon content (90.4%) and the lowest oxygen content (8.7%), correlating with the low silica content. The spectrum of ARP exhibits signals at 1280 $cm^{-1}$ and 1030 $cm^{-1}$ corresponding to P=O and P–O–C bonds, respectively,[40] confirming the functionalization of the carbon surface with phosphate groups. These functionalities may not only serve as anchoring points for metal nanoparticles, but could also introduce acidity, potentially catalysing side reactions.[80] XPS analyses further support this, revealing a distinct increase in the surface phosphorus content, consistent with incorporation of phosphate functionalities. The broad FT-IR signal centred at around 3400 $cm^{-1}$, observed across all samples, is likely attributable to –OH functionalities or residual water adsorbed on the carbon surface.[81] Additionally, a signal corresponding to the stretching of aliphatic C–H bonds is observed at around 2900 $cm^{-1}$ across all carbon samples.[82]

Table 4 XPS composition of the main elements present on the surface of non-activated and activated biochar samples. The complete table can be found in Table S1†

| Sample | C [%] | O [%] | Si [%] | N [%] | P [%] |
|---|---|---|---|---|---|
| BR | 73.4 | 19.3 | 5.7 | 1 | — |
| ARS | 69.2 | 21.9 | 8.1 | 0.6 | — |
| ARC | 75.8 | 18.5 | 4.4 | — | |
| ARK | 90.4 | 8.7 | 0.7 | 0.1 | — |
| ARP | 24.3 | 48.9 | 8.3 | — | 18.0 |

Notably, XPS provides additional insights into surface composition changes induced by activation. Steam activation led to a decrease in the surface carbon content (from 73.4% in BR to 69.2% in ARS) confirming the oxidation of the superficial carbon,[83] with a collateral increase in silica concentration, a trend even more pronounced in ARP, highlighting the aggressive nature of phosphoric acid activation. Conversely, ARC exhibited a surface composition similar to raw biochar, indicating the lower reactivity of $CO_2$ as an activating agent.[84] Interestingly, while elemental analysis indicates a lower bulk oxygen concentration on ARK, XPS confirms that oxygen remains concentrated on the surface (8.7%). Since surface oxygen groups are known to serve as anchoring sites for metal nanoparticles, influencing their dispersion and catalytic behaviour,[73,85] their presence on activated char surfaces could make these materials valuable as supports for catalytic applications (Table 5).

Since surface oxygen groups are known to serve as anchoring sites for metal nanoparticles, influencing their dispersion and catalytic behaviour,[73,85] their presence on activated char surfaces could make these materials valuable as supports for catalytic applications.

The deconvolution of the C 1s spectra provided deeper insights into the distribution of oxygen functionalities across the samples, as shown in Fig. 4 and Table 7. The C 1s core level spectrum of BR was deconvoluted into 7 main contributions, while ARS and ARC gave six contributions, and ARP and ARK gave five.

Notably, the peak at ~283 eV, associated with Si–C bonds, is absent both in ARK and ARP, suggesting that chemical activation played a crucial role in breaking these bonds, which were initially present in BR and likely formed during high temperature pyrolysis.

The disappearance of Si–C bonds in ARK is consistent with its significantly lower silica content, due to the leaching by KOH activation. On the other hand, ARP exhibited a high silica content, yet no Si–C bonds are detected. This suggested that phosphoric acid activation chemically modified the material and led to a structural reorganization. This was evidenced by SEM-EDX analysis (Fig. 2), showing that silica is no longer present in distinct layers but is rather homogeneously dispersed, indicating a complete disruption

Table 5 $pH_{PZC}$ of the biochar samples calculated by the pH drift method

| Sample | $pH_{PZC}$ |
|---|---|
| ARS | 7.1 |
| ARC | 6.3 |
| ARK | 7.4 |
| ARP | 2.3 |

**Table 6** Pd effective content determined through MP-AES

| Sample | Pd wt% |
|---|---|
| Pd/ARS | 0.64 |
| Pd/ARC | 0.68 |
| Pd/ARK | 0.77 |
| Pd/ARP | 0.16 |

of C–Si bonding. Besides the Si–C contribution, the relative intensities of the oxygen-functionalized carbon species provide further insights into the impact of activation. The C 1s spectra show significant variations in oxygen-containing functional groups (C–O, C=O, O–C=O) across the samples. Before activation, the dominant peak at 285.1 eV corresponds to C–C and C–H bonds.[86] Following activation, the peak at 284.7 eV attributed to C=C bonds becomes the most pronounced. Other common peaks across all samples are found at 286.5 eV for C–O of hydroxyl and lactone groups, 287.9 eV for C=O (ketone groups), and 289.5 eV for O–C=O (carboxylic groups).[87]

Overall, the oxygen functionality trend follows ARC > ARS > ARP > ARK, highlighting the different roles of activation agents in modifying the surface chemistry, which is an important factor on biochar's suitability as a catalyst support. ARK exhibits the lowest intensity for these oxygen functionalities, aligning with its overall lower oxygen content detected by both elemental analysis and XPS. The C=O peak (~287.9 eV) accounts for 2.3% in ARK, while the O–C=O peak (−289.3 eV) is present at only 2.8%, indicating low oxygen functionalization.[88] Among the samples, ARS and ARK exhibit the highest contribution for C=O functionalities.

In contrast, ARS and ARC exhibit the highest proportions of oxygen-related peaks, indicating a more oxidized surface compared to the other samples. ARS features a peak at ~287.5 eV, attributed to C=O functionalities, contributing 4.9%, and a peak at ~289.3 eV related to O–C=O functionalities, at 6.6%, while ARC presents C–O (~286.7 eV) at 6.1% and O–C=O (~288.9 eV) at 4.5%.[89] These values suggest that steam and $CO_2$ activation, although less efficient in increasing surface area compared to KOH, significantly enhanced the oxygen functionalization of the biochar surface. This modification is likely to influence metal interactions and catalytic performances. Interestingly, ARP presents slightly lower oxygen functionalities than ARS and ARC, with C–O (~286.7 eV) at 4.8% and O–C=O (~288.9 eV) at 3.1%. The formation of C–P bonds is expected;[90] however, the peaks overlap with the C–O bonds. Considering the amounts of oxygen, 63 at%, and phosphorus, 10.2 at%, the contribution of photoelectrons emitted from C–P bonding to the C 1s peak was not considered. While phosphoric acid is known to promote oxidation, it also facilitates phosphorus incorporation, as evidenced by FT-IR, which likely reduces the relative proportion of oxygen groups. This suggests that ARP underwent significant structural modifications due to activation, resulting in a distinct surface chemistry compared to the other biochar samples. The differences highlighted by XPS analysis were further confirmed by $pH_{PZC}$ measurements. The $pH_{PZC}$ (point of zero charge) represents the pH at which the net surface charge is zero, and it is a crucial parameter in catalyst preparation. While an appropriate functionalization is essential for metal anchoring and coordination, it also modifies the total charge of the material, influencing the electrostatic interaction of metal species, which exist in the ionic form.[91] The presence of acidic functional groups (*e.g.* carboxyl, phenol, phosphate) lowers the $pH_{PZC}$, increasing the attraction toward cationic species, whereas basic groups raise the $pH_{PZC}$, promoting interaction with anionic complexes. Extreme pH values can result in strong electrostatic interactions that may hinder metal adsorption[92] by decreasing the adsorption equilibrium constant.[93] The PZC values of ARS and ARK are relatively similar (7.1 and 7.4, respectively), while ARC exhibited a slightly lower PZC (6.3).

## Characterization of the catalysts and catalytic performance

The effective palladium content in the catalysts was determined using microwave plasma-atomic emission spectroscopy (MP-AES), and the values are reported in

**Table 7** Peak position and area of C 1s spectra of the non-activated and activated biochar samples

| Sample | C–Si | C=C | C–C | C–O–H, C–O–C | C=O | O–C=O | π |
|---|---|---|---|---|---|---|---|
| | Peak position (eV) | | | | | | |
| | Peak area (%) | | | | | | |
| BR | 283.9 | 284.6 | 285.1 | 286.5 | 288.0 | 289.4 | 292.9 |
| | 8.8 | 26.4 | 50.3 | 6.1 | 2.7 | 3.1 | 2.6 |
| ARS | 282.9 | 284.5 | 285.5 | | 287.5 | 289.3 | 291.7 |
| | 7.5 | 52.2 | 25.3 | | 4.9 | 6.6 | 3.5 |
| ARC | 283.5 | 284.5 | 285.1 | 286.7 | | 288.9 | 291.0 |
| | 14.7 | 59.0 | 12.7 | 6.1 | | 4.5 | 3.0 |
| ARK | — | 284.7 | 286.1 | | 287.9 | 289.3 | 291.8 |
| | | 81.2 | 10.4 | | 2.3 | 2.8 | 1.9 |
| ARP | — | 284.6 | 285.1 | 286.7 | | 288.9 | 291.1 |
| | | 80.8 | 10.0 | 4.8 | | 3.1 | 1.2 |

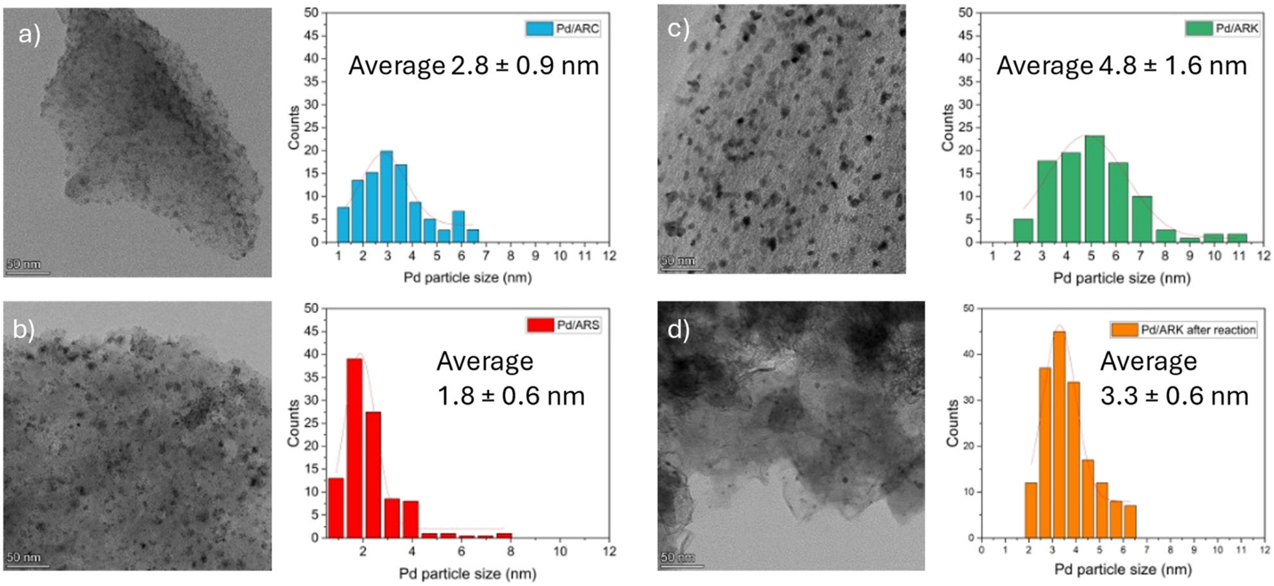

**Fig. 5** TEM images and Pd NP size distribution of a) Pd/ARC, b) Pd/ARS, c) Pd/ARK and d) Pd/ARK after the reaction.

Table 6. The measured values for Pd/ARS, Pd/ARC and Pd/ARK were consistent with the nominal loading of 0.75 wt%, indicating efficient Pd deposition. However, Pd/ARP exhibited a significantly lower palladium uptake of only 0.16 wt%, which can be attributed to its low surface area and very low $pH_{PZC}$, which is significantly different from the pH at which the deposition–precipitation is conducted. This could have resulted in a high ionic strength, which in turn could have reduced the palladium adsorption constant,[92] and hindered the metal uptake.

TEM images, reported in Fig. 5, reveal uniformly distributed nanoparticles for Pd/ARK, Pd/ARC, and Pd/ARS, though with varying average particle size in the order Pd/ARK > Pd/ARC > Pd/ARS. Pd/ARK exhibited the biggest particle size, with an average size of approximately 4.8 nm. Pd/ARS displayed smaller nanoparticles with a narrower size

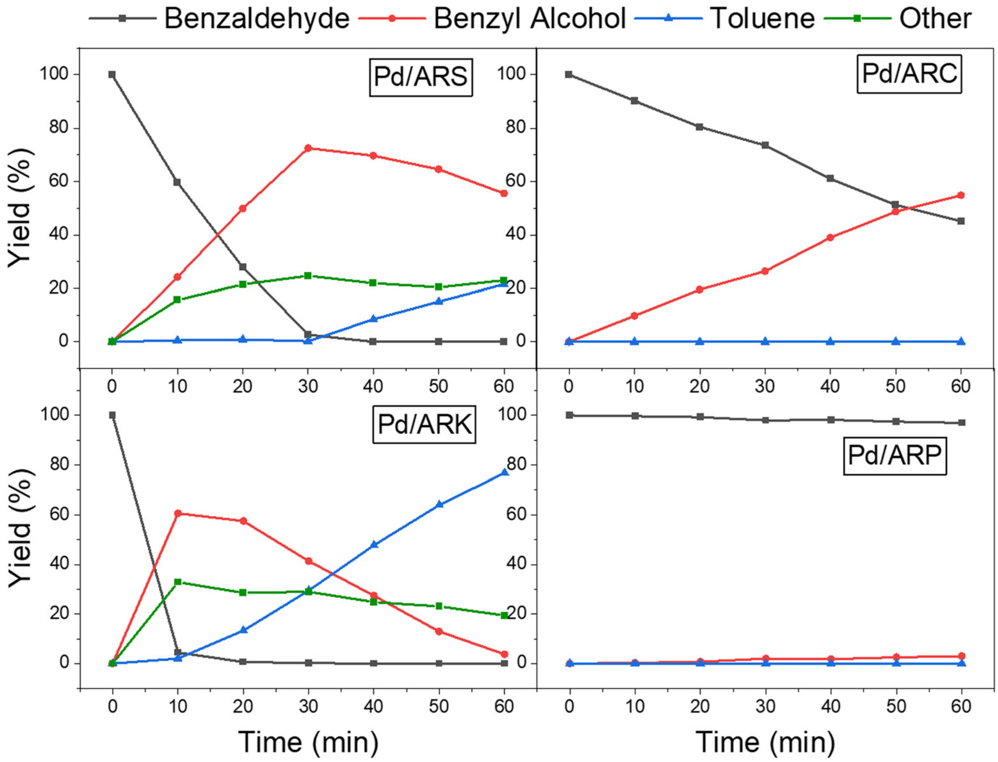

**Fig. 6** Reaction profiles over the different catalysts.

**Table 8** Productivity of the catalysts. Conversion and yield calculated after 60 minutes, and TOF calculated after 10 minutes

| Sample | Conversion (%) | Yield of hydrogenated products (BAL + TOL) (%) | TOF ($s^{-1}$) |
|---|---|---|---|
| Pd/ARS | 100 | 77<br>(56 + 21) | 0.58 |
| Pd/ARC | 55 | 37<br>(37+0) | 0.38 |
| Pd/ARK | 100 | 81<br>(4 + 77) | 3.22 |
| Pd/ARP | 3 | 3<br>(3 + 0) | 0.06[a] |

[a] The TOF for Pd/ARP was calculated without considering distribution, as it was not possible to determine through TEM imaging.

distribution, centered at 1.9 nm, though some agglomerates were observed, as reported in Fig. S3.† Pd/ARC showed a more homogeneous dispersion of particles ranging from 1 to 8 nm. Notably, TEM images did not reveal any visible Pd nanoparticles for Pd/ARP (Fig. S2†), confirming the low metal content detected by MP-AES. These findings were further supported by TPR measurements reported in Fig. S4,† which showed a negative peak at around 70 °C (attributed to the decomposition of Pd β-hydride species[94]) in all samples except for Pd/ARP.

The catalytic performance of the synthesized materials was evaluated in the hydrogenation of benzaldehyde, a tandem reaction where benzaldehyde is first hydrogenated to benzyl alcohol, followed by its conversion to toluene *via* hydrogenolysis.[95] The reaction, conducted in ethanol, can also involve acid sites on the catalyst, which activate the carbonyl group, promoting ethanol addition and forming hemiacetal or acetal intermediates.[96] However, these reactions are reversible, as the intermediates undergo hydrogenolysis followed by hydrogenation over the palladium sites.[96]

As shown in Fig. 6 and Table 8, Pd/ARK exhibited the highest activity, with a turnover frequency of 3.22 $s^{-1}$, significantly surpassing Pd/ARS (0.58 $s^{-1}$) and Pd/ARC (0.38 $s^{-1}$). Due to its low metal loading, which prevented accurate determination of particle size distribution, the TOF for Pd/ARP was calculated based on metal wt%. However, it resulted in a much lower value of 0.06 $s^{-1}$.

These variations in activity evidenced the strong correlation between the catalytic performance and the activation process, which influenced both textural properties and surface composition.

A linear correlation was observed between the surface area and catalytic activity. A high surface area with accessible micropores and small mesopores enhances the dispersion of the active phase.[97] The best-performing support, ARK, exhibited the highest surface area (2635 $m^2$ $g^{-1}$), followed by ARS (423 $m^2$ $g^{-1}$) and ARC (367 $m^2$ $g^{-1}$). ARP, which had the lowest surface area (112 $m^2$ $g^{-1}$), also displayed the lowest catalytic activity. Its limited surface area likely affected metal/support interactions, resulting in Pd/ARP having a low metal content. While surface area is a crucial factor, chemical functionalization also played a role, albeit in a more complex manner. Oxygen-containing functional groups are essential for anchoring metal nanoparticles, yet their impact on the catalytic performance is more complex and multifaceted.[98,99] CHNS, XPS and FTIR analyses indicated that ARK had the lowest density of heteroatoms and functional groups among the samples. However, both Pd/ARK and Pd/ARS exhibited the presence of more oxidized functionalities, particularly carbonyl groups, which are known to promote nanoparticle nucleation and may contribute to improved metal dispersion.[100] These characteristics likely contributed to the superior performance of these two catalysts, compared to the others.

Nevertheless, an excess of oxygen functionalization can negatively impact dispersion. Lazzarini *et al.* demonstrated that a high concentration of oxygen-containing functional groups can hinder metal dispersion on the surface, leading to agglomeration.[101] As a matter of fact, Pd/ARK, with the lowest amount of oxygen functionalities, exhibited the largest average nanoparticle size (4.8 nm), but no signs of agglomeration, contributing to its superior performance. In contrast, Pd/ARS, with a higher abundance of O-based functional groups, despite having smaller average particles (1.9 nm), showed some degree of agglomeration, which may partially explain its lower TOF. Moreover, the relationship between particle size and catalytic activity is not straightforward, as the optimal size varies depending on the reaction.[97,98] For example, Binder *et al.* reported that Pd nanoparticles of 3–4 nm led to the highest TOF for ethene hydrogenation.[102] The superior performance of Pd/ARK in this study suggests that its particle size of 4.7 nm remains within the optimal range, and the homogeneous distribution all over the support surface further contributes to enhanced activity.

This aligns with findings by Suh *et al.*, who observed that while oxygen functionalities improve metal dispersion, they do not necessarily enhance catalytic activity.[103] Instead, the distribution of metal particles, electronic properties and textural characteristics are the key determinants of performance.

The TOF values obtained in this study are consistent with those reported in the literature and, in some cases, even exceed them. Typical TOF values for benzaldehyde hydrogenation range from 0.05 to 1.08 $s^{-1}$.[104–108] Notably,

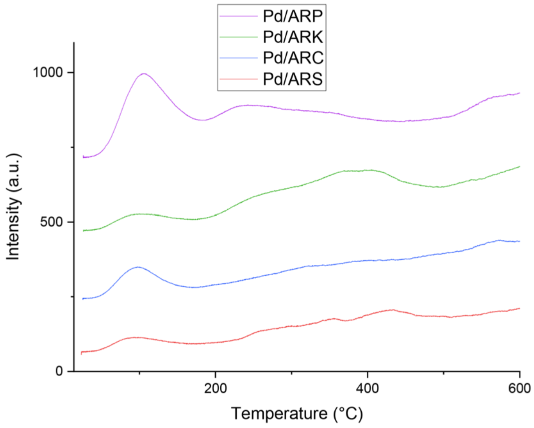

**Fig. 7** Ammonia-TPD profile of the different catalysts.

even under mild conditions (25 °C and atmospheric pressure), the TOF values obtained in this work remain higher than previously reported values. Also, values reported for more traditional palladium-on-carbon catalysts are consistent with those observed in the current work ($0.79\ s^{-1}$,[109] $0.29\ s^{-1}$ (ref. 70)), confirming that biochar produced from waste materials, when properly activated, can be equally or even more efficient. This suggests that rice husk could be used as an alternative sustainable carbon source for catalytic applications.

Besides the activity, also the reaction pathway and product distribution are influenced by catalyst properties. The selectivity trends further emphasize the influence of textural and electronic properties on catalytic behaviour. Pd/ARK exhibited the highest selectivity toward hydrogenation/hydrogenolysis pathways, achieving a 77% yield of toluene after 60 minutes. In contrast, Pd/ARS progressed more slowly, and achieved only 21% yield of toluene after 1 hour, favouring a high yield of benzyl alcohol (56%). This suggests that Pd/ARS effectively facilitates hydrogenation but with slower hydrogenolysis, leading to intermediate accumulation. During the reaction, side-products such as diethoxy methylbenzene and ethoxy methylbenzene can be formed *via* ethanol addition to benzaldehyde.[56] These intermediates result from the reversible formation of hemiacetals and acetals, promoted by acid sites and metal–support interactions.[96] For Pd/ARK, the selectivity to hydrogenation products is 63% after 10 minutes and increases to 80.6% after 60 minutes, suggesting the conversion of side products and the reversibility of the reaction. For Pd/ARC and Pd/ARP, no toluene was detected after 60 minutes of reaction, and Pd/ARP, with the very low activity, exhibited only 3% conversion and complete selectivity towards BALOH. As the formation of side products is often promoted by acidic sites,[110] ammonia temperature-programmed desorption ($NH_3$-TPD) analysis was performed to assess the acidity of the catalysts.

Fig. 7 presents the TPD profiles for all the catalysts. Two main desorption peaks are observed across the samples. A peak at around 100 °C, attributed to weak acid sites,[111] is present in all the catalysts, with the higher intensity recorded for Pd/ARP, followed by Pd/ARC. These two catalysts were activated using acid treatments ($H_3PO_4$ and $CO_2$, respectively), which effectively introduced a greater amount of acid sites. Pd/ARP also exhibits a second peak at around 220 °C, associated with weak-to-medium acid sites. Notably, a distinct peak at around 400 °C is visible for Pd/ARK and Pd/ARS and can be ascribed to acid sites of medium strength.[111] Considering the low functionalization of ARK, as reported in the CHNS analysis (Table 2), the acidity detected on this catalyst might be due to the metal–support interactions, as these peaks are already reported for Pd-based catalysts in the literature.[112,113] It is worth noting that the presence of side products was detected only in the case of Pd/ARS and Pd/ARK, suggesting that weak acid sites do not promote side products under the reaction conditions employed, but the presence of stronger acid sites is detrimental to hydrogenated product selectivity.

After the reaction, the best performing catalyst was recovered by filtration. To understand changes in the catalyst, TEM imaging of the spent catalyst was performed, as reported in Fig. 5. The analysis shows that the catalyst retained metal dispersion.

## Conclusions

Rice husk, a significant agricultural by-product, was utilized to produce activated biochar for Pd-based catalysts. Different activation methods were applied to tailor the textural and surface properties of the materials, optimizing metal–support interactions and dispersion. This study highlights that textural properties play a fundamental role in determining catalytic performance, demonstrating that a well-developed micro- and mesoporous structure is essential for high catalytic activity. Among the tested catalysts, Pd/ARK exhibited the best catalytic performance, achieving a TOF of $3.22\ s^{-1}$ and a toluene yield of ~77%, after one hour. This superior activity was attributed to its exceptionally high surface area of $2635\ m^2\ g^{-1}$ and a well-balanced combination of micro- and mesopores, which facilitated Pd nanoparticle dispersion and minimized agglomeration. Additionally, the moderate surface functionalization of Pd/ARK resulted in a neutral $pH_{PZC}$, further promoting stable metal–support interactions. Although physical activation is often preferred for its sustainability, as it avoids the use of strong acids or bases, this study demonstrates that chemical activation can generate high-performance carbon supports from waste biomass. To enhance the sustainability of chemical activation, potassium recycling strategies can be explored. Furthermore, the silica recovered from rice husk during activation presents an opportunity for reuse as a precursor in silica-based materials, offering a more sustainable and resource-efficient alternative to conventional silica sources. These findings provide valuable insights into the design of biochar-supported Pd catalysts, highlighting the crucial role of the activation agent in tailoring textural properties, metal–support interactions, and electronic effects to achieve optimal catalytic performance in selective hydrogenation reactions.

## Data availability

The authors confirm that the data supporting the findings of this study are available within the article and its ESI.†

## Author contributions

Lilia Longo: methodology, writing – original draft preparation. Davide Baldassin: investigation, data curation, writing – original draft preparation. Alessandro Di Michele: formal analysis. Carla Bittencourt: formal analysis. Federica Menegazzo: validation, review & editing. Michela Signoretto: supervision, conceptualization, resources.

## Conflicts of interest

There are no conflicts to declare.

## Acknowledgements

The MIUR (Italian Ministry for Education, University and Research) is gratefully acknowledged for the financial support (doctoral scholarships) of the Ph.D. program of University Ca' Foscari Venice. Riseria delle Abbadesse is acknowledged for supplying the rice husk. Dr. Beatrice Muzzi of ICCOM-CNR of Florence is gratefully acknowledged for the TEM analyses.

## Notes and references

1 S. Schmidt and D. Laner, *Waste Manage.*, 2025, **198**, 137–150.

2 T. Keijer, V. Bakker and J. C. Slootweg, *Nat. Chem.*, 2019, **11**, 190–195.

3 N. Tripathi, C. D. Hills, R. S. Singh and C. J. Atkinson, *npj Clim. Atmos. Sci.*, 2019, **2**, 1–10.

4 A. M. S. Chun and I. E. Brisson, *Ground Rules in Humanitarian Design*, John Wiley & Sons, 2015.

5 M. Mofijur, T. M. I. Mahlia, J. Logeswaran, M. Anwar, A. S. Silitonga, S. M. A. Rahman and A. H. Shamsuddin, *Energies*, 2019, **12**, 4116.

6 B. Phan, T. L. Duong, V. Nguyen, T. Tran, M. Nguyen, H. L. Nguyen, D. Nguyen and L. Luu, *Biomass Bioenergy*, 2014, **62**, 74–81.

7 S. S. Shukla, R. Chava, S. Appari, A. Bahurudeen and B. V. R. Kuncharam, *J. Environ. Chem. Eng.*, 2022, **10**, 106899.

8 A. K. Vuppaladadiyam, S. S. V. Vuppaladadiyam, A. Sahoo, S. Murugavelh, E. Anthony, T. Bhaskar, Y. Zheng, M. Zhao, H. Duan, Y. Zhao, E. Antunes, A. K. Sarmah and S.-Y. Leu, *Sci. Total Environ.*, 2023, **857**, 159155.

9 V. S. Prabhudesai and R. Vinu, *Top. Catal.*, 2023, **66**, 405–419.

10 A. Saravanan and P. S. Kumar, *Environ. Res.*, 2022, **214**, 113857.

11 P. Bhavani, D. Praveen Kumar, M. Hussain, T. M. Aminabhavi and Y.-K. Park, *Chem. Eng. J.*, 2022, **434**, 134743.

12 X. Hu and M. Gholizadeh, *J. Energy Chem.*, 2019, **39**, 109–143.

13 Z. Luo, S. Wang, Y. Liao, J. Zhou, Y. Gu and K. Cen, *Biomass Bioenergy*, 2004, **26**, 455–462.

14 K. Qian, A. Kumar, H. Zhang, D. Bellmer and R. Huhnke, *Renewable Sustainable Energy Rev.*, 2015, **42**, 1055–1064.

15 S. Dutta, A. Bhaumik and K. C.-W. Wu, *Energy Environ. Sci.*, 2014, **7**, 3574–3592.

16 W. Zheng, B. K. Sharma and N. Rajagopalan, *Sustainable Agriculture Grant Program Illinois Department of Agriculture*, 2010.

17 M. Ahmad, A. U. Rajapaksha, J. E. Lim, M. Zhang, N. Bolan, D. Mohan, M. Vithanage, S. S. Lee and Y. S. Ok, *Chemosphere*, 2014, **99**, 19–33.

18 C. Wen, T. Liu, D. Wang, Y. Wang, H. Chen, G. Luo, Z. Zhou, C. Li and M. Xu, *Prog. Energy Combust. Sci.*, 2023, **99**, 101098.

19 A. P. Khedulkar, B. Pandit, V. D. Dang and R. Doong, *Sci. Total Environ.*, 2023, **869**, 161441.

20 H. Lyu, Q. Zhang and B. Shen, *Chemosphere*, 2020, **240**, 124842.

21 B. İnan, A. T. Koçer and D. B. Özçimen, *J. Anal. Appl. Pyrolysis*, 2023, **173**, 106095.

22 F. Menegazzo, E. Ghedini, L. Longo, D. Baldassin, S. Taghavi and M. Signoretto, *Chem. Eng. Trans.*, 2024, **109**, 367–372.

23 R. Pereira Lopes and D. Astruc, *Coord. Chem. Rev.*, 2021, **426**, 213585.

24 J. Liu, J. Jiang, Y. Meng, A. Aihemaiti, Y. Xu, H. Xiang, Y. Gao and X. Chen, *J. Hazard. Mater.*, 2020, **388**, 122026.

25 N. L. Panwar and A. Pawar, *Biomass Convers. Biorefin.*, 2022, **12**, 925–947.

26 H. W. Lee, Y.-M. Kim, S. Kim, C. Ryu, S. H. Park and Y.-K. Park, *Carbon Lett.*, 2018, **26**, 1–10.

27 C.-H. Hsiao, S. Gupta, C.-Y. Lee and N.-H. Tai, *Appl. Surf. Sci.*, 2023, **610**, 155560.

28 R.-Z. Wang, D.-L. Huang, Y.-G. Liu, C. Zhang, C. Lai, X. Wang, G.-M. Zeng, X.-M. Gong, A. Duan, Q. Zhang and P. Xu, *Chem. Eng. J.*, 2019, **371**, 380–403.

29 J. Pallarés, A. González-Cencerrado and I. Arauzo, *Biomass Bioenergy*, 2018, **115**, 64–73.

30 J. Cheng, C. Bi, X. Zhou, D. Wu, D. Wang, C. Liu and Z. Cao, *Langmuir*, 2023, **39**, 14119–14129.

31 L. Leng, Q. Xiong, L. Yang, H. Li, Y. Zhou, W. Zhang, S. Jiang, H. Li and H. Huang, *Sci. Total Environ.*, 2021, **763**, 144204.

32 L. Cao, I. K. M. Yu, D. C. W. Tsang, S. Zhang, Y. S. Ok, E. E. Kwon, H. Song and C. S. Poon, *Bioresour. Technol.*, 2018, **267**, 242–248.

33 J. Wang and S. Wang, *J. Cleaner Prod.*, 2019, **227**, 1002–1022.

34 S. Zhang, Q. Zhang, S. Zhu, H. Zhang and X. Liu, *Energy Sources, Part A*, 2021, **43**, 282–290.

35 V. Gargiulo, F. Di Natale and M. Alfe, *J. Environ. Chem. Eng.*, 2024, **12**, 113497.

36 L. N. Hakkim and L. Nebhani, *Surf. Interfaces*, 2024, **51**, 104505.

37 S. Kumar, R. Singh, K. Bansal, R. K. Diwan and S. K. Shukla, *Mater. Sci. Eng., B*, 2024, **309**, 117632.

38 G. Chu, J. Zhao, Y. Huang, D. Zhou, Y. Liu, M. Wu, H. Peng, Q. Zhao, B. Pan and C. E. W. Steinberg, *Environ. Pollut.*, 2018, **240**, 1–9.

39 I. Neme, G. Gonfa and C. Masi, *Heliyon*, 2022, **8**, e11940.

40 A. M. Puziy, O. I. Poddubnaya, A. Martínez-Alonso, F. Suárez-García and J. M. D. Tascón, *Carbon*, 2002, **40**, 1493–1505.

41 S. H. Dhawane and G. Halder, in *Advances in Feedstock Conversion Technologies for Alternative Fuels and Bioproducts*, ed. M. Hosseini, Woodhead Publishing, 2019, pp. 199–220.

42 J. Lee, K.-H. Kim and E. E. Kwon, *Renewable Sustainable Energy Rev.*, 2017, **77**, 70–79.

43 K. Velusamy, J. B. Isabel, S. Periyasamy, A. Thiruvenkadam, H. Ravikumar, S. K. Gupta and E. A. López-Maldonado, *J. Taiwan Inst. Chem. Eng.*, 2024, 105732.

44 M. A. Stoffels, F. J. R. Klauck, T. Hamadi, F. Glorius and J. Leker, *Adv. Synth. Catal.*, 2020, **362**, 1258–1274.

45 G. A. Filonenko, R. van Putten, E. J. M. Hensen and E. A. Pidko, *Chem. Soc. Rev.*, 2018, **47**, 1459–1483.

46 L. He, Y. Wang, H. Gao, Z. Liu and Z. Xie, *RSC Adv.*, 2021, **11**, 33646–33652.

47 K. A. Sanoja-López and R. Luque, *Inorg. Chem. Commun.*, 2024, **170**, 113277.

48 P. Udomsap, S. Meesiri, N. Chollacoop and A. Eiad-Ua, *Nanomaterials*, 2021, **11**, 1431.

49 F. Menegazzo, P. Canton, F. Pinna and N. Pernicone, *Catal. Commun.*, 2008, **9**, 2353–2356.

50 S. Capelli, S. Cattaneo, M. Stucchi, B. D. Vandegehuchte, A. Chieregato, A. Villa and L. Prati, *Catalysts*, 2022, **12**, 251.

51 R. M. Mironenko, O. B. Belskaya, T. I. Gulyaeva, M. V. Trenikhin, A. I. Nizovskii, A. V. Kalinkin, V. I. Bukhtiyarov, A. V. Lavrenov and V. A. Likholobov, *Catal. Today*, 2017, **279**, 2–9.

52 C. González, P. Marín, F. V. Díez and S. Ordóñez, *Ind. Eng. Chem. Res.*, 2016, **55**, 2319–2327.

53 H. Shafaghat, I.-G. Lee, J. Jae, S.-C. Jung and Y.-K. Park, *Chem. Eng. J.*, 2019, **377**, 119986.

54 Y. Yang, X. Xu, H. He, D. Huo, X. Li, L. Dai and C. Si, *Int. J. Biol. Macromol.*, 2023, **242**, 124773.

55 G. Bagnato, M. Signoretto, E. Ghedini, F. Menegazzo, X. Xi, G. H. ten Brink, B. J. Kooi, H. J. Heeres and A. Sanna, *New J. Chem.*, 2023, **47**, 9440–9450.

56 L. Longo, S. Taghavi, M. Riello, E. Ghedini, F. Menegazzo, A. Di Michele, G. Cruciani and M. Signoretto, *Catal. Today*, 2023, **420**, 114038.

57 X. Chen, Y. Fang, J. Zhu, F. Wang, T. Zhao and D. Fan, *Proceedings of the International Conference on Electronics, Mechanics, Culture and Medicine*, Atlantis Press, 2016, pp. 362–367.

58 T.-K.-T. Nguyen, T.-B. Nguyen, W.-H. Chen, C.-W. Chen, A. Kumar Patel, X.-T. Bui, L. Chen, R. R. Singhania and C.-D. Dong, *Bioresour. Technol.*, 2023, **371**, 128593.

59 G. Chu, J. Zhao, Y. Huang, D. Zhou, Y. Liu, M. Wu, H. Peng, Q. Zhao, B. Pan and C. E. W. Steinberg, *Environ. Pollut.*, 2018, **240**, 1–9.

60 T. Lear, R. Marshall, J. Antonio Lopez-Sanchez, S. D. Jackson, T. M. Klapötke, M. Bäumer, G. Rupprechter, H.-J. Freund and D. Lennon, *J. Chem. Phys.*, 2005, **123**, 174706.

61 Standard Test Method for pH of Activated Carbon, https://www.astm.org/d3838-05r17.html, (accessed February 17, 2025).

62 M. Pashai Gatabi, H. Milani Moghaddam and M. Ghorbani, *J. Mol. Liq.*, 2016, **216**, 117–125.

63 M. M. Alam, M. A. Hossain, M. D. Hossain, M. a. H. Johir, J. Hossen, M. S. Rahman, J. L. Zhou, A. T. M. K. Hasan, A. K. Karmakar and M. B. Ahmed, *Processes*, 2020, **8**, 203.

64 J. Lee, J. Kim and T. Hyeon, *Adv. Mater.*, 2006, **18**, 2073–2094.

65 S. Amin, M. Ahmed, E. El-Sayed and M. Abadir, *American-Eurasian Journal of Sustainable Agriculture*, 2013, **7**, 413–419.

66 K. Qian, A. Kumar, K. Patil, D. Bellmer, D. Wang, W. Yuan and R. L. Huhnke, *Energies*, 2013, **6**, 3972–3986.

67 P. Salimi, S. Tieuli, S. Taghavi, E. Venezia, S. Fugattini, S. Lauciello, M. Prato, S. Marras, T. Li, M. Signoretto, P. Costamagna and R. P. Zaccaria, *Green Chem.*, 2022, **24**, 4119–4129.

68 C. Toles, S. Rimmer and J. C. Hower, *Carbon*, 1996, **34**, 1419–1426.

69 M. Jagtoyen and F. Derbyshire, *Carbon*, 1998, **36**, 1085–1097.

70 F. Pinna, F. Menegazzo, M. Signoretto, P. Canton, G. Fagherazzi and N. Pernicone, *Appl. Catal., A*, 2001, **219**, 195–200.

71 C. H. Bartholomew and R. J. Farrauto, *Fundamentals of Industrial Catalytic Processes*, John Wiley & Sons, 2011.

72 O. Oginni, K. Singh, G. Oporto, B. Dawson-Andoh, L. McDonald and E. Sabolsky, *Bioresour. Technol. Rep.*, 2019, **7**, 100266.

73 A. E. Aksoylu, M. Madalena, A. Freitas, M. F. R. Pereira and J. L. Figueiredo, *Carbon*, 2001, **39**, 175–185.

74 B. Hazmi, U. Rashid, Z. N. Akhlisah, S. Chaowamalee, C. Ngamcharussrivichai and M. J. Sabater, *Biomass Bioenergy*, 2025, **194**, 107607.

75 S. F. Vaughn, J. A. Kenar, B. Tisserat, M. A. Jackson, N. Joshee, B. N. Vaidya and S. C. Peterson, *Ind. Crops Prod.*, 2017, **97**, 260–267.

76 H. T. Phuong, Md. A. Uddin and Y. Kato, *J. Biobased Mater. Bioenergy*, 2015, **9**, 439–446.

77 J. Zhang, H. Fu, X. Lv, J. Tang and X. Xu, *Biomass Bioenergy*, 2011, **35**, 464–472.

78 J. P. Borrajo, S. Liste, J. Serra, P. González, S. Chiussi, B. León, M. P. Amor, H. O. Ylänen and M. Hupa, *Key Eng. Mater.*, 2004, **254–256**, 23–26.

79 E. Herth, R. Zeggari, J.-Y. Rauch, F. Remy-Martin and W. Boireau, *Microelectron. Eng.*, 2016, **163**, 43–48.

80 L. J. Kennedy, J. J. Vijaya and G. Sekaran, *Ind. Eng. Chem. Res.*, 2004, **43**, 1832–1838.

81 T.-H. Liou and S.-J. Wu, *J. Hazard. Mater.*, 2009, **171**, 693–703.
82 T.-H. Liou, *Carbon*, 2004, **42**, 785–794.
83 J. Alvarez, G. Lopez, M. Amutio, J. Bilbao and M. Olazar, *Ind. Eng. Chem. Res.*, 2015, **54**, 7241–7250.
84 M. Sevilla and R. Mokaya, *Energy Environ. Sci.*, 2014, **7**, 1250–1280.
85 C. Prado-Burguete, A. Linares-Solano, F. Rodríguez-Reinoso and C. S.-M. de Lecea, *J. Catal.*, 1989, **115**, 98–106.
86 T. Cai, X. Liu, J. Zhang, B. Tie, M. Lei, X. Wei, O. Peng and H. Du, *J. Cleaner Prod.*, 2021, **281**, 125390.
87 B. Singh, Y. Fang, B. C. C. Cowie and L. Thomsen, *Org. Geochem.*, 2014, **77**, 1–10.
88 C. Bittencourt, C. Navio, A. Nicolay, B. Ruelle, T. Godfroid, R. Snyders, J.-F. Colomer, M. J. Lagos, X. Ke, G. Van Tendeloo, I. Suarez-Martinez and C. P. Ewels, *J. Phys. Chem. C*, 2011, **115**, 20412–20418.
89 S. Acosta, J. Casanova Chafer, A. Sierra Castillo, E. Llobet, R. Snyders, J.-F. Colomer, M. Quintana, C. Ewels and C. Bittencourt, *Appl. Sci.*, 2019, **9**, 5342.
90 B. Peng, Y. Xu, K. Liu, X. Wang and F. M. Mulder, *ChemElectroChem*, 2017, **4**, 2140–2144.
91 J. Park and J. R. Regalbuto, *J. Colloid Interface Sci.*, 1995, **175**, 239–252.
92 X. Hao, S. Barnes and J. R. Regalbuto, *J. Catal.*, 2011, **279**, 48–65.
93 J. R. Regalbuto, A. Navada, S. Shadid, M. L. Bricker and Q. Chen, *J. Catal.*, 1999, **184**, 335–348.
94 G. Neri, M. G. Musolino, C. Milone, D. Pietropaolo and S. Galvagno, *Appl. Catal., A*, 2001, **208**, 307–316.
95 A. Saadi, Z. Rassoul and M. M. Bettahar, *J. Mol. Catal. A: Chem.*, 2000, **164**, 205–216.
96 M. Arai, A. Obata and Y. Nishiyama, *J. Catal.*, 1997, **166**, 115–117.
97 J. Wang and S. Kaskel, *J. Mater. Chem.*, 2012, **22**, 23710–23725.
98 O. M. Wilson, M. R. Knecht, J. C. Garcia-Martinez and R. M. Crooks, *J. Am. Chem. Soc.*, 2006, **128**, 4510–4511.
99 A. Ejsmont, K. Kadela, G. Grzybek, T. Darvishzad, G. Słowik, M. Lofek, J. Goscianska, A. Kotarba and P. Stelmachowski, *ACS Appl. Mater. Interfaces*, 2023, **15**, 5148–5160.
100 B. Bowden, M. Davies, P. R. Davies, S. Guan, D. J. Morgan, V. Roberts and D. Wotton, *Faraday Discuss.*, 2018, **208**, 455–470.
101 A. Lazzarini, R. Pellegrini, A. Piovano, S. Rudić, C. Castan-Guerrero, P. Torelli, M. R. Chierotti, R. Gobetto, C. Lamberti and E. Groppo, *Catal. Sci. Technol.*, 2017, **7**, 4162–4172.
102 A. Binder, M. Seipenbusch, M. Muhler and G. Kasper, *J. Catal.*, 2009, **268**, 150–155.
103 D. J. Suh, P. Tae-Jin and I. Son-Ki, *Carbon*, 1993, **31**, 427–435.
104 X.-F. Guo, D.-Y. Jang, H.-G. Jang and G.-J. Kim, *Catal. Today*, 2012, **186**, 109–114.
105 Y. Song, U. Sanyal, D. Pangotra, J. D. Holladay, D. M. Camaioni, O. Y. Gutiérrez and J. A. Lercher, *J. Catal.*, 2018, **359**, 68–75.
106 Y. Hao, C. Pischetola, F. Cárdenas-Lizana and M. A. Keane, *Catal. Lett.*, 2020, **150**, 881–887.
107 A. Proto, R. Cucciniello, A. Genga and C. Capacchione, *Catal. Commun.*, 2015, **68**, 41–45.
108 P. Liu, Y. Zhao, R. Qin, S. Mo, G. Chen, L. Gu, D. M. Chevrier, P. Zhang, Q. Guo, D. Zang, B. Wu, G. Fu and N. Zheng, *Science*, 2016, **352**, 797–800.
109 S. Capelli, S. Cattaneo, M. Stucchi, B. D. Vandegehuchte, A. Chieregato, A. Villa and L. Prati, *Catalysts*, 2022, **12**, 251.
110 J. N. Hall and P. Bollini, *ACS Catal.*, 2020, **10**, 3750–3763.
111 A. M. Venezia, V. L. Parola, B. Pawelec and J. L. G. Fierro, *Appl. Catal., A*, 2004, **264**, 43–51.
112 T. Romero, L. Melo, M. Esparragoza, R. Ávila, A. Moronta, G. Carruyo and L. García, *Revista UIS Ingenierías*, 2023, **22**, 25–34.
113 M. Pirmoradi, N. Janulaitis, R. J. Gulotty Jr. and J. R. Kastner, *ACS Omega*, 2020, **5**, 7836–7849.
114 U. Iriarte-Velasco, I. Sierra, L. Zudaire and J. L. Ayastuy, *Food Bioprod. Process.*, 2016, **98**, 341–353.